This is a Just Accepted version, keep updated with https://doi.org/10.26599/OCEAN.2026.9470024
OCEAN 2026, 2, 9470024

Research Article

Spatially heterogeneous superwettability in groove surfaces: anchored plastron for underwater drag reduction

Zhitao Huang, Yiwei Hu, Zhaoxi Liang, Shicai Zhu, Liran Ma*, Jianbin Luo

State Key Laboratory of Tribology in Advanced Equipment, Tsinghua University, Beijing 100084, China

Address correspondence to Liran Ma, maliran@tsinghua.edu.cn

Received: March 31, 2026 / Revised: April 29, 2026 / Accepted: May 5, 2026

ABSTRACT

The air layer, known as a plastron, on superhydrophobic surfaces plays a crucial role in underwater drag reduction. However, stabilizing the plastron in complex turbulent flow conditions is a significant challenge, which impairs its effectiveness in drag reduction. This study proposes a streamwise groove structure with heterogeneous superwettability (HS-groove). The surface of the groove is treated through alkaline etching and water bath processes to form micro-needle-like crystals, resulting in superhydrophilicity with a water contact angle (CA) near 0° on the top surface. The interior of the groove is modified with hexadecyltrimethoxysilane (HDTMOS), imparting superhydrophobicity, with a CA exceeding 160° and a water roll-off angle (RA) of approximately 2°. This HS-groove structure demonstrates superior underwater plastron stability and drag reduction performance compared to traditional superhydrophobic grooves. Under continuous water flow, the plastron within grooves exhibited long-term persistence, with the maximum duration reaching 7.3 h and the corresponding drag reduction rates ranging from 17.2% to 46.4%

in the pipeline. The strong surface energy barrier of the HS-groove enables effective plastron retention, leading to drag reduction performance superior to that of pure superhydrophobic grooves. This study offers novel insights and potential applications in underwater drag reduction technologies.

KEYWORDS

superwettability, groove, plastron, drag reduction

1 Introduction

Superhydrophobicity refers to superwettability characterized by a static water contact angle (CA) greater than 150° and a water roll-off angle (RA) less than 10° [1,2]. The unique chemical properties and micro-nanostructure of the superhydrophobic surface impart ultra-low adhesion to water, making them extremely difficult to be wetted [3–5]. As a result, superhydrophobic surfaces have been increasingly studied with the aim of effectively being applied in underwater drag reduction, pipeline transportation, and other fields over the past two decades [6–9]. Previous studies have demonstrated that the effectiveness of underwater drag reduction on superhydrophobic surfaces primarily depends on the air layer (plastron) maintained on the surface [10–12]. However, the stability of superhydrophobicity and the durability of the plastron have long been challenging problems. Therefore, achieving a stable and durable plastron has become a critical research direction in superhydrophobic drag reduction [13,14]. Existing optimization strategies can be categorized into two approaches.

The first category concerns surface structure. Studies have demonstrated that streamwise superhydrophobic grooves outperform other surface structures in terms of underwater drag reduction and are beneficial for maintaining underwater air layers. Nie et al [15]. used photolithography to dry etch streamwise microtrenches on a silicon wafer, which were then

modified with 1H,1H,2H,2H-perfluorodecyltriethoxysilane (FAS-17) to create superhydrophobic grooves. Based on small pipeline experiments, they measured the drag reduction rates corresponding to microtrenches of different widths and lengths. When the width of the microtrenches increased from 45μm to 180μm, the drag reduction rate increased from 9.6% to 19.9% . Their study shows that the microtrenches ensure the mechanical stability of the air, and the gas can automatically dewet when it comes into contact with new air after continuous dissolution. Additionally, Hemeda et al [16]. employed numerical simulations to examine the impact of superhydrophobic grooves on the behavior and stability of the internal gas layer, further establishing a quantitative relationship between the air-liquid interface (AWI) pressure balance and the groove shape parameters, initial gas volume, etc. Their findings provided mathematical guidance for stabilizing gas in superhydrophobic grooves.

Furthermore, based on surface physicochemical properties, some researchers have proposed anchoring plastrons by coupling two extreme types of wettability: hydrophilic (CA < 90°) and hydrophobic (CA > 90°) surfaces, using surface energy barriers to maintain the AWI. Inspired by the floating fern Salvinia molesta to anchor the AWI, Speichermann-Jaegel et al [17]. used stereolithography 3D printing and surface modification to fabricate a columnar array surface with a hydrophilic top (Poly-(4-vinylpyridine)) and a superhydrophobic (Teflon) base. Laser scanning confocal microscopy (LSCM) revealed that this structure significantly improved the stability of the air layer, nearly doubling the snap-off pressure at the air-liquid contact line. Hu et al [18]. used a mask spraying method to prepare a surface with alternating superhydrophobic and hydrophilic stripes. After gas injection, the surface anchored the solid-liquid-gas three-phase contact line (TCL), forming a stable air ring on the Taylor-Couette flow rotor and achieving a drag reduction rate of up to 77.2%.

The aforementioned studies optimize the fixation of underwater air layers from the

perspectives of surface structure and physicochemical properties. However, their limitations remain evident. For structure-based approaches, although streamwise grooves improve the mechanical stability of the plastron, their constraint on the air layer is still limited, making it difficult to suppress gas loss over time. For wettability-based approaches, while hydrophilic-hydrophobic coupling enhances the pressure stability of the air layer under static or Taylor-Couette flow conditions, its durability under complex flowing conditions is often insufficient, and such surfaces may not perform effectively as drag-reducing interfaces. It's conceivable that effectively combining both approaches could further enhance the durability of the underwater plastron and stabilize the drag reduction. Moreover, if the wettability contrast could be further increased, i.e., coupling superhydrophilicity (CA < 10°) and superhydrophobicity, the surface could achieve even better performance. However, achieving such heterogeneous superwettability on 3D structures is challenging, as the modification routes for hydrophilic and hydrophobic regions are often incompatible.

Young's equation describes the wettability of an ideal solid surface by relating the contact angle θ to the interfacial tensions γ as shown in Fig. 6f [19,20]:

$$cos\theta = (\gamma_{sg} - \gamma_{sl})/\gamma_{gl} \quad (1)$$

Where γ_{sg}, γ_{sl}, and γ_{gl} are the solid-gas, solid-liquid, and gas-liquid surface tensions, respectively. For rough surfaces, the apparent contact angle θ_w can be described by the Wenzel model by introducing the roughness coefficient r [21]:

$$cos\theta_w = rcos\theta \quad (2)$$

This indicates that surface wettability is jointly determined by intrinsic surface chemistry and surface roughness, with roughness acting as an amplification factor [22–25]. The intrinsic wettability, governed by surface physicochemical properties, can be tuned via chemical modification [4,26,27], whereas the roughness factor r is determined by the microstructure.

Therefore, for a given microstructure, modifying the surface chemistry can lead to markedly different wettability states, i.e., enhancing either hydrophilicity or hydrophobicity. This provides the basis for realizing heterogeneous wettability on identical structures.

Based on this, we propose a method for fabricating streamwise grooves with heterogeneous superwettability. By subjecting laser-machined aluminum alloy substrates with macroscopic grooves to alkaline etching and water bath treatment, needle-like microstructures with superhydrophilic properties are grown on the surface. The grooves are then modified by superhydrophobic immersion to create partial superhydrophobicity. This surface integrates superhydrophilic-superhydrophobic heterogeneity with macroscopic streamwise grooves, enabling enhanced plastron stability through the combined effects of wettability contrast and groove confinement, and thereby achieving more durable and reliable underwater drag reduction than conventional designs.

2 Experimental Materials and Methods

2.1 Materials

Grooves with varying widths, spacing, and depths were laser-engraved on 6061 aluminum alloy substrates (38 mm × 20 mm × 8 mm), with representative groove dimensions shown in Fig. S1. The samples were ultrasonically cleaned for 30 minutes using petroleum ether, followed by anhydrous ethanol. Hexyltrimethoxysilane (HDTMOS, ≥ 85%) was purchased from Shanghai Macklin Biochemical Technology Co., Ltd., NaCl and NaOH was purchased from Shanghai Acmec Biochemical Technology Co., Ltd. (AR). Petroleum ether, anhydrous ethanol, and acetic acid were sourced from Shanghai Titan Technology Co., Ltd. (AR), and n-Heptane (99.5%, AR) was purchased from Beijing Inokai Technology Co., Ltd.

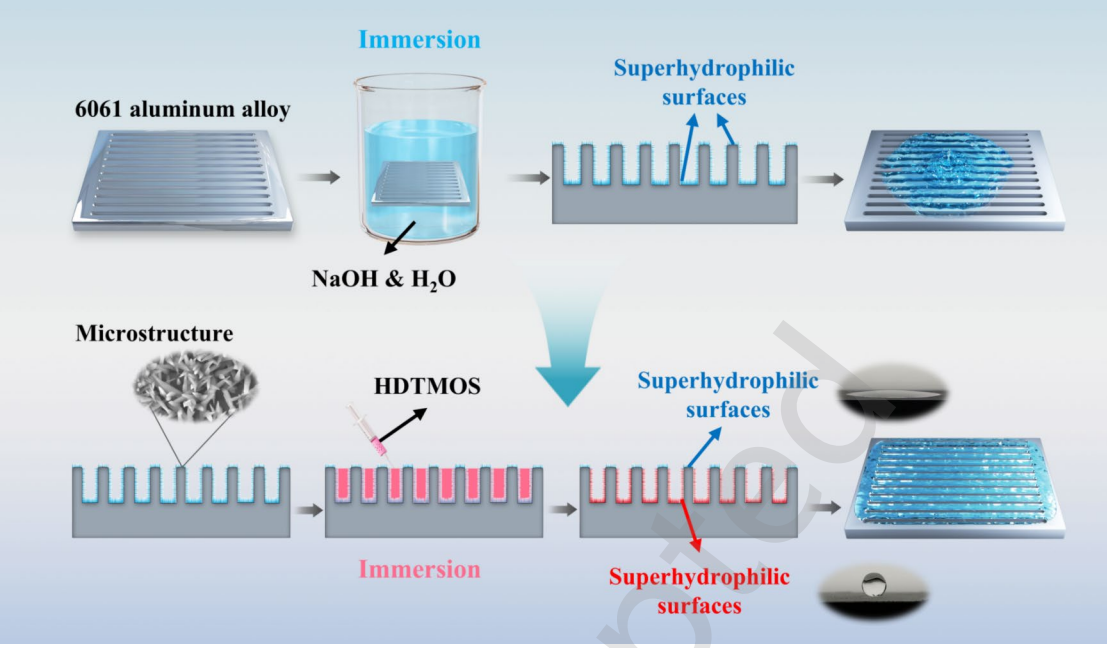

Fig. 1. Schematic illustration of the preparation process and surface morphology of the HS-groove.

2.2 Preparation of the Surface with Superwettability

The cleaned and dried 6061 aluminum alloy groove substrates were immersed in a 0.1M NaOH solution for 10 minutes, with the solution temperature was maintained at 70°C using an oil bath. The alkaline-etched samples were subsequently immersed in deionized water for 40 minutes, with the water temperature maintained at 90°C using an oil bath. Finally, the samples were placed in deionized water and allowed to cool to room temperature for 24 hours. After soaking, the samples were removed and dried in a constant temperature oven at 80°C for 1 hour. After alkaline etching and water bath treatment, a dense needle-like crystal structure forms on the aluminum surface, resulting in a superhydrophilic wetting state.

HDTMOS (1 ml), deionized water (2 ml), and acetic acid (1 ml) were dissolved in n-Heptane (25 ml), then stirred to form a hydrophobic modification solution. The solution was subsequently injected into the superhydrophilic grooves using a syringe. To ensure the liquid level and protect the superhydrophilic surface, the modified solution was injected quantitatively, and the ridge

surface of the groove was completely covered by a thin layer of PDMS. After 12 hours of immersion, the solution was dried in a constant temperature oven at 80°C for 2 hours. After modification, the grooves become superhydrophobic, whereas the remaining surfaces remain superhydrophilic. The preparation processes for the superhydrophilic/superhydrophobic surfaces and HS-groove are illustrated in Fig. 1.

2.3 Characterization

The wettability of the superhydrophilic/superhydrophobic surfaces was characterized using a video contact angle meter (OCA25, Dataphysics, Germany), with an experimental water drop volume of 5 μL. The surface morphology of the hydrophilic and hydrophobic treated samples was examined using a field emission scanning electron microscope (FE-SEM; GeminiSEM 300, Zeiss, Germany). The elemental composition was analyzed using energy dispersive X-ray spectroscopy (EDS; compatible with the FE-SEM). The chemical composition of the samples was analyzed using Fourier transform infrared spectroscopy (FT-IR; Nexus 870, Thermofisher, USA) to confirm the presence of the target chemical bonds after modification. X-ray photoelectron spectroscopy (XPS; ESCALAB 250Xi, Thermofisher, USA) was employed to characterize the chemical environment of the target elements on surfaces with varying wettability. The 3D morphology of grooves of varying geometries was obtained using a white light interferometer (NeXView, USA). A high-speed camera was employed to capture the dynamic behavior of droplets on surfaces with varying superwettability.

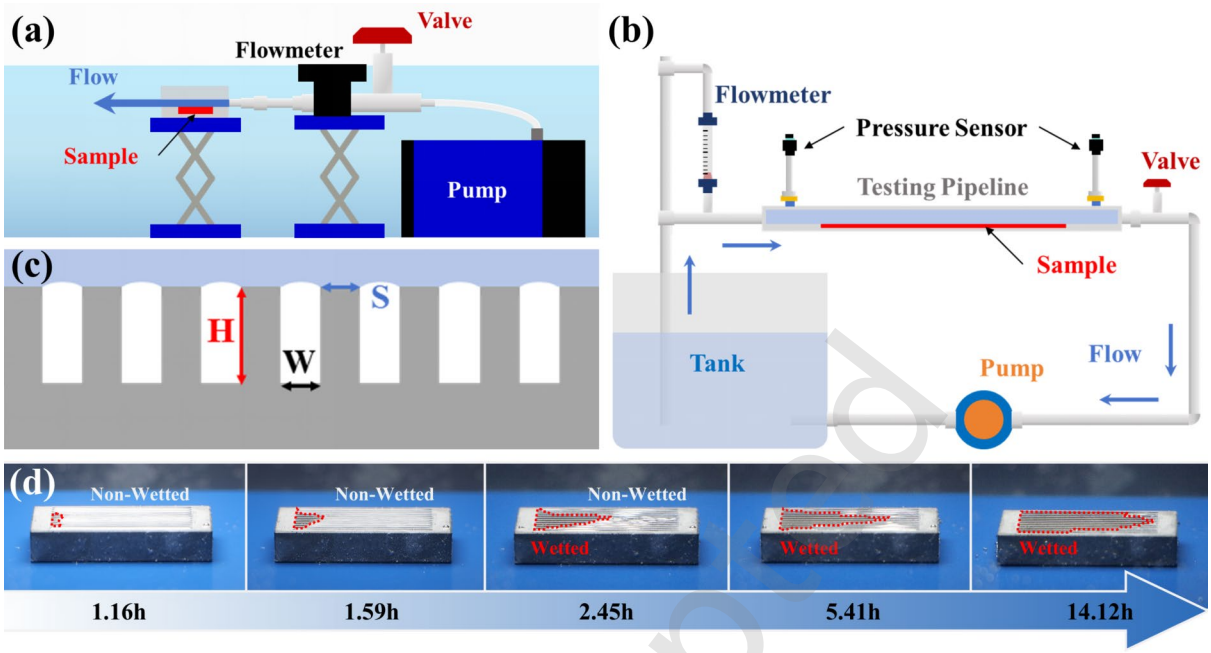

Fig. 2. Experiments on the durability and drag reduction performance of the plastron in the HS-groove. (a) Schematic diagram of the plastron scour resistance test device. (b) Schematic diagram of the pipeline drag test device. (c) Definition of the groove width (W), depth (H), and spacing (S). (d) Wetting states of the plastron at various scouring durations.

2.4 Plastron Durability and Drag Reduction

A water pump circulation tank was employed to assess the durability of the air layer trapped in the HS-grooves. The sample was positioned on a platform in a water tank (Fig. 2a), with a flow rate range from 0.25 m/s to 1.50 m/s. The duration and residual volume of the air layer were recorded during continuous underwater flushing of multiple grooves to evaluate the durability of air within HS-grooves of varying geometries. The durability of the superhydrophilic and superhydrophobic flat surfaces was also assessed through flow scouring and sandpaper wear tests (Fig. S3). Mechanical durability was further evaluated via ultrasonic durability test (Fig. S12). The samples were fully immersed in 0 °C ice water, 50 °C water, and 3.5 wt% NaCl solution, respectively, and subjected to ultrasonication at 60 W and 40 kHz. The contact angles (CAs) and

rolling angles (RAs) were measured after different exposure times. Each group of experiments was repeated 3 times and the average value was taken. The durability of the air layer within the HS-groove under still water immersion is presented in Fig. S9a.

Furthermore, drag reduction tests were conducted using a circulating pipeline, as shown in Fig. 2b. The drag reduction caused by the streamwise HS-grooves was quantified using the pressure drop method. The samples were closely arranged in a custom-designed slot within an acrylic pipe. Before measurement, the pressure sensors were calibrated in both air and still water conditions, the pressure and pressure difference values were zeroed respectively. The flow was adjusted to a corresponding velocity. Sensors recorded pressure data at the inlet and outlet of the test section. After the flow field and sample surface conditions stabilized, sensor data were collected over a 30-second period to calculate the pressure differential and compare the drag reduction efficiencies of the different samples, each group of experiments was repeated 3 times. Both durability and drag reduction tests were performed in rectangular channels with a cross-section of 20 mm × 10 mm.

To characterize the relative importance of inertial versus capillary forces, the groove width (W) was nondimensionalized using the Weber number:

$$W^+ = \frac{\rho u^2 W}{\sigma} \tag{3}$$

Where ρ is the fluid density, u is the flow velocity, and σ (0.0728 N/m) is the surface tension. The dimensions of the groove depth and spacing were respectively represented by H/W and S/W. Together with the dimensionless width (W^+), these parameters for experiment are summarized in Table 1.

2.5 Computational Fluid Dynamics (CFD) Analysis

CFD simulations were conducted using Ansys Fluent software. Fig. 7a-b shows the 3D

computational domain, consisting of the liquid domain (L_F = 500 mm, H_F = 115 mm, W_F = 12 mm) and the groove region (L_g = 38 mm, H = 5 mm, W = 1 mm, S = 1 mm). The horizontal distance x_g between the start of the groove and the inlet ($x = 0$) is 422 mm, with the coordinate direction shown in the figure. Initially, the groove is filled with air, and the upper fluid domain is filled with water. The Navier-Stokes equations were solved using the shear stress transport model k-omega (SST k-ω) and the pseudo-transient method. Simultaneously, the volume of fluid (VOF) method was used to accurately simulate the interface and interaction between the two fluids. A velocity inlet with a turbulence intensity of 5% and a pressure outlet of the computational domain were set. Both sides of the flow field were symmetrical boundaries, and all other boundaries were no-slip walls. The water contact angles on the superhydrophilic and superhydrophobic walls were set to 5 ° and 155 ° , respectively. To ensure computational accuracy, a mesh size of approximately 5.7×10^6 was used, and the distribution of wall y^+ in the groove region is shown in Fig. S10. The grid independence, time-step convergence verification, and the comparison with the experimental simulation results are shown in the Fig. S11.

3 Results and Discussion

3.1 Surface morphology and Superwettability

Alkali etching is one of the most effective methods for achieving surfaces with extreme wettability [28]. In an alkaline aqueous environment, metal surfaces are etched to form micro-nanostructures, while the concurrent growth of metal crystals often further regularizes and compacts the surface microstructure [29]. Additionally, the hydroxyl groups on the surface of the hydroxide crystals impart excellent hydrophilicity to the surface after alkaline etching, thus creating a superhydrophilic surface (SHPhi) [30]. As shown in Fig. 3a-b, needle-like clusters approximately 10 μm in length grow on 6061 aluminum alloy under the combined effects of NaOH etching and water bath treatment. The infrared spectroscopy signal in Fig. 3c reveals that the

superhydrophilic surface exhibits the same O-H infrared peak as that of $Al(OH)_3$, confirming the presence of $Al(OH)_3$ on the surface. This indicates that an $Al(OH)_3$ gel layer forms on the aluminum alloy surface during alkaline etching, followed by the further growth of $Al(OH)_3$ into micron-sized needle-like crystals in water. The chemical properties of the needle-like microstructure and the surface hydroxyl groups contribute to the excellent superhydrophilicity of the surface, as shown in Fig. 3e, where the CA approaches 0°.

The superhydrophilic surface was further modified to become superhydrophobic by immersion. The modification solution primarily consisted of hexadecyltrimethoxysilane (HDTMOS), a substance known for low surface energy due to its long carbon chain and methyl end groups . During the immersion process, HDTMOS hydrolyzed and bonded to the hydroxyl groups on the superhydrophilic surface. After drying and dehydration, the surface underwent chemical assembly. As shown in Fig. 3c, the modified superhydrophobic surface (SHPho) exhibited the same C-H infrared peak as HDTMOS when compared to the superhydrophilic surface, demonstrating the successful modification. The well-defined needle-like microstructure and the low surface energy chemical properties of the superhydrophobic modification resulted in excellent superhydrophobicity, as shown in Fig. 3f-g, with CA and RA of 160.6° and 2.0°, respectively.

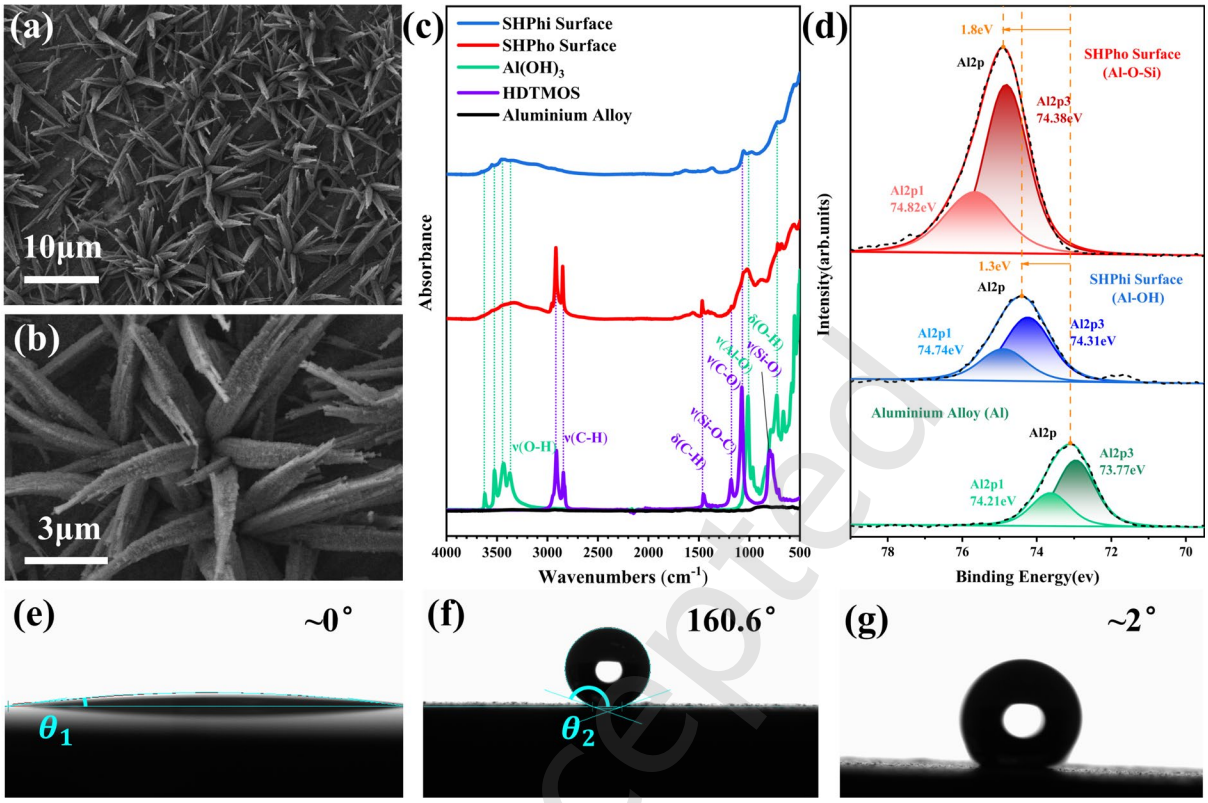

Fig. 3. Characterization of the physicochemical properties of HS-groove surfaces. (a, b) SEM images of needle-like microstructures at 1000× and 3000× magnifications. (c) FT-IR spectra and (d) XPS spectra of surfaces with different superwettabilities and reference materials. (e, f) Optical images of water CA on the superhydrophilic and superhydrophobic surfaces, respectively. (g) Water RA on the superhydrophobic surface.

The X-ray photoelectron spectroscopy (XPS) results for the original aluminum alloy substrate, superhydrophilic surface, and superhydrophobic surface are shown in Fig. S4. The all-element survey spectrum reveals that the superhydrophilic surface has more pronounced Al and O signals than the aluminum alloy surface. This reflects the formation of $Al(OH)_3$ during the superhydrophilic modification process, while impurity elements are removed to a certain extent. On the other hand, the superhydrophobic surface exhibits an additional Si signal, a relatively enhanced C signal, and a decrease in the relative values of the Al and O signals, indicating that the

silane molecules have successfully bonded to the surface. In the narrow XPS spectrum in Fig. 3d, the chemical state of the Al element is shown in detail. It can be observed that the binding energy of the Al element gradually increases from the aluminum alloy to the superhydrophilic surface, and then to the superhydrophobic surface, with each modification resulting in a corresponding chemical shift. This is due to the increasing electronegativity of the hydroxyl group (-OH) and the silane molecule (-O-Si-) , which affects the electron density of the Al outer layer [31,32]. Al undergoes a transition from its elemental form to binding with the hydroxyl group (-OH) and then to binding with the silane (-O-Si-). The more electronegative groups significantly reduce the electron density of the Al outer layer, thus further weakening the electron shielding effect. As a result, the binding energy of Al on the superhydrophilic surface, primarily existing in the form of $Al(OH)_3$, increases by 1.3 eV. Furthermore, upon binding to silane, the Al on the superhydrophobic surface undergoes an additional positive chemical shift (1.8 eV).

The two surfaces show minimal difference under SEM, but EDS spectra reveal variations in the proportions of chemical elements on the two surfaces (Fig. S5a-b). This demonstrates that the experiment successfully achieved superhydrophilic/superhydrophobic modifications on the same substrate and microstructure. Fig. S6 shows the dynamics of a water droplet freely falling on the two surfaces. The droplet on the superhydrophilic surface spreads rapidly, while the droplet on the superhydrophobic surface bounces and remains stationary, appearing non-wetting.

The superhydrophilic and superhydrophobic surfaces were also evaluated through experiments shown in Fig. S3. The CA of the superhydrophilic surface remained below 10° after 60 minutes of water impact at a flow rate of 1.50 m/s. The superhydrophobic surface also maintained superhydrophobicity under these conditions, with CA greater than 150° and RA less than 10°. In a sandpaper wear test shown in Fig. S3b, both surfaces maintained excellent superwettability after 10 cycles of friction (10 cm reciprocating per cycle). This demonstrates the

excellent mechanical stability of the microstructure and chemical composition of both the superhydrophilic and superhydrophobic surfaces. The durability of the surface superwettability was further evaluated by ultrasonic shear tests under representative immersion conditions, including 3.5 wt% NaCl solution (simulated seawater), ice water at 0 °C, and hot water at 50 °C (exceeding the upper limit of typical ocean temperatures). Ultrasonic treatment was conducted at a power of 60 W and a frequency of 40 kHz for 2 h. As shown in Fig. S12, a relatively pronounced change in surface wettability was observed in simulated seawater. After 2 h of treatment, the CA of the superhydrophobic surface decreased to ~150°, with RA increasing to ~6°, while a slight increase in CA was observed for the superhydrophilic surface. In contrast, no significant change was observed in ice water, whereas the hot-water environment led to slight degradation of superhydrophobicity, although superhydrophilicity remained well preserved.

3.2 Groove Dimension and Plastron Durability

The fabrication principle of the HS-grooves is shown in Fig. 1. The surfaces inside the grooves are superhydrophobic, while the surfaces between the grooves are superhydrophilic. The width and depth of the superhydrophobic groove interior are denoted by W and H, respectively, while the width of the superhydrophilic spacer is denoted by S, as shown in Fig. 2c. Optical microscopy images are provided in Fig. S2. Due to the spatial distribution of superwettability, the surface effectively retains air within the grooves when submerged underwater, as shown in Fig. 2d. To compare and investigate the effects of HS-grooves with varying dimensions on gas retention underwater, this study conducted 5 × 3 × 3 groups of gas layer durability gradient experiments, each with a controlled single dimension variable. The experimental setups are illustrated in Fig. 2a.

Table 1 Groove dimensionless width (u = 1m/s), depth, and spacing.

Dimension	Value				
W/mm	0.5	0.8	1.0	1.2	1.5
W^+	6.9	11.0	13.7	16.5	20.6
H/W	1/2/5	1/2/5	1/2/5	1/2/5	1/2/5
S/W	0.2/0.5/1	0.2/0.5/1	0.2/0.5/1	0.2/0.5/1	0.2/0.5/1

During the experiment, the grooves were continuously subjected to scouring and shearing by water with a flow rate of 1.0 m/s. As shown in Fig. 2d, the air volume in the groove initially remained nearly constant (steady state) with increasing scouring time, then decreased rapidly (unsteady state), and ultimately approached complete depletion after prolonged scouring. The steady-state duration of plastron in the central grooves was used as the criterion. When the gas loss within the grooves exceeds 5%, the entrapped gas is regarded as having transitioned into an unsteady state. The effective gas retention time was therefore defined as the time required to reach this threshold, which was measured in 3 repeated experiments and averaged for comparison. Fig. 4a-c show the gas durability test results for HS-grooves with dimensionless widths of 6.9, 11.0, 13.7, 16.5, and 20.6, respectively. The results indicate that, with other variables held constant, the steady-state duration of plastron exhibits a positive correlation with H/W and a negative correlation with W^+, and this relationship is consistently observed for each individual S/W group. Overall, the groove with S/W = 1.0 exhibits the best plastron durability, followed by S/W = 0.5, and the group with S/W = 0.2 generally shows the shortest duration. Among the 5 groups with different W^+ values, the maximum gas scour resistance duration was achieved at H/W = 5 and S/W = 1.0. When W^+ = 6.9, the HS-groove sustained a stable plastron state (gas loss < 5%) for over 1.1 h. As a control, the underwater plastron durability of fully superhydrophobic grooves (SHPho groove) was also evaluated, as shown in Fig. S7a. For clarity, a subset of representative geometric parameters was selected for comparison (H/W = 5, S/W = 1.0; H/W = 2, S/W = 0.5;

H/W = 1, S/W = 0.2). The results demonstrate that HS-grooves exhibit superior gas durability underwater compared to SHPho grooves, with gas retention generally improving exceeding 30%.

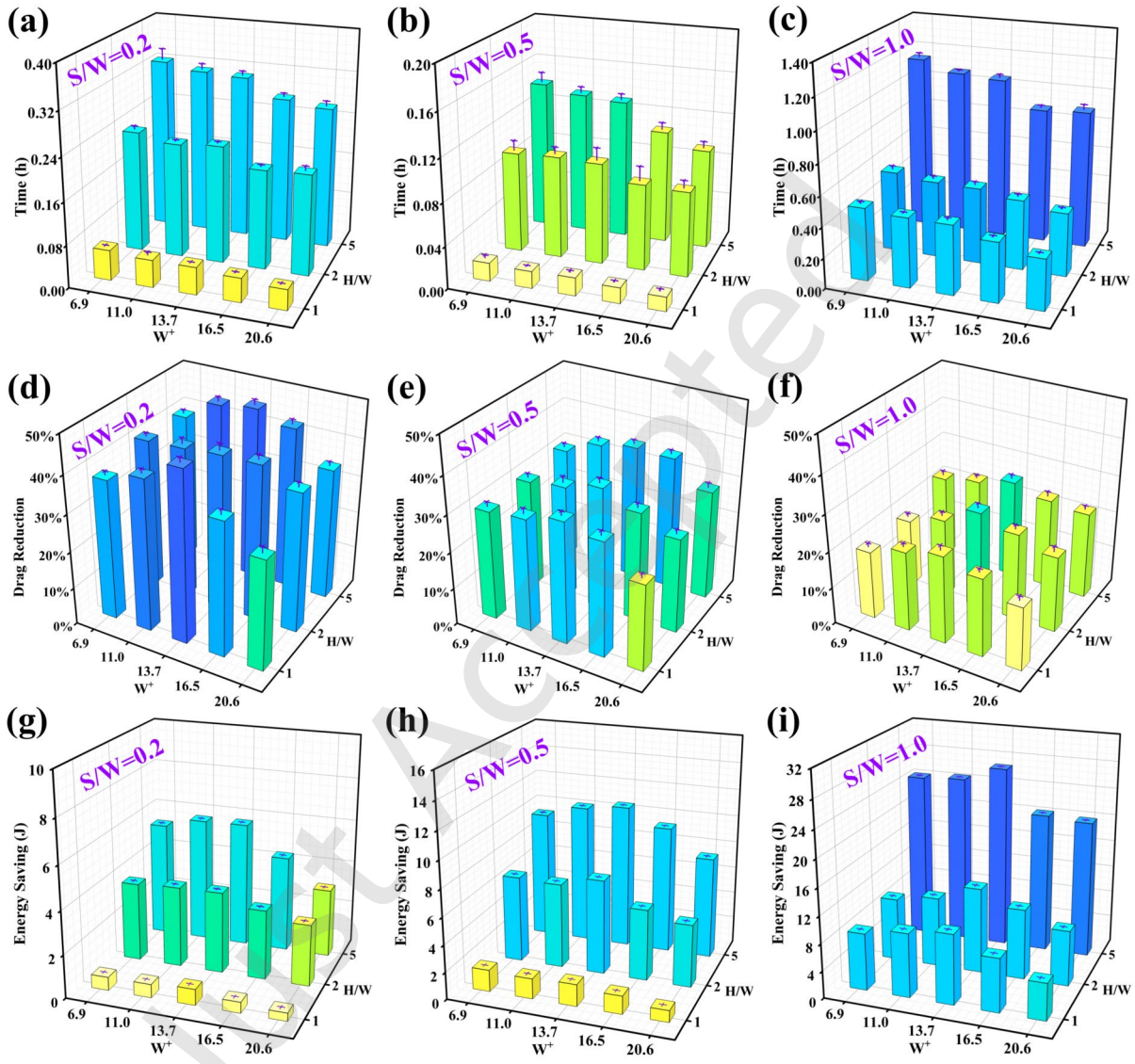

Fig. 4. Distribution of HS-groove plastron durability, drag reduction, and energy saving performance with respect to the groove dimensions. (a-c) Steady-state duration of the plastron for grooves with S/W of 0.2, 0.5, and 1.0. (d-f) Drag reduction rates for grooves with S/W of 0.2, 0.5, and 1.0 in pipeline. (g-i) Overall energy savings for grooves with S/W of 0.2, 0.5, and 1.0.

Fig. S8a-c also illustrates the effect of the individual geometric dimensions on the gas durability. The steady-state duration of plastron shows a positive correlation with both the H/W

and S/W. The groove depth H determines the initial gas storage capacity upon submergence. With increasing H, the transmission of pressure fluctuations and shear stresses from the external flow to the trapped gas is progressively attenuated within the groove, thereby enhancing gas retention and prolonging the steady-state duration. In addition, hydrophilic surfaces exhibit stronger intermolecular interactions with water than hydrophobic ones, an effect that is further amplified for superhydrophilic surfaces. Such surfaces promote the formation of a stable solid-liquid interface, which anchors the TCL at the groove edges and provides an energy barrier against gas loss. As S/W increases, i.e., with a wider superhydrophilic spacing between grooves, the steady-state duration of plastron is significantly prolonged, highlighting the positive role of the superhydrophilic spacer in reinforcing TCL pinning and stabilizing the entrapped gas. A larger W^+ is generally detrimental to gas retention, as it increases the area of the AWI exposed to flow-induced pressure fluctuations, shear stresses, and gas diffusion, thereby accelerating gas depletion. When the groove width becomes excessively large (W^+ = 16.5 and 20.6) , these effects are further amplified, limiting the sustained retention of gas within the groove. In summary, within the test system shown in Fig. 2a, optimal gas retention performance is achieved at W^+ = 6.9, H/W = 5, and S/W = 1.0, where the gas loss remains below 5% for over 1.16 h under continuous water flow at 1.0 m/s. Under lower flow velocity conditions (u = 0.25 m/s), the maximum plastron steady-state duration is further extended to 7.3 h at W^+ = 0.43, with the same geometric ratios of S/W = 1.0and H/W = 5. Since W^+ is jointly governed by the groove width W and the flow velocity u, these results collectively indicate that enhanced plastron stability favors smaller W^+ in combination with larger S/W and H/W within the investigated parameter range.

Fig. 5a presents the dependence of the steady-state plastron duration within HS-grooves and SHPho grooves (S/W = 1.0, H/W = 5.0) on the dimensionless width W^+ in logarithmic coordinates. The curve corresponding to HS-grooves consistently lies above that of SHPho

grooves, indicating superior plastron stability. For a steady-state duration exceeding 0.1 h, HS-grooves maintain this level even at $W^+ = 46.4$, whereas for SHPho-grooves the duration drops below this threshold when $W^+ > 40$. This suggests that the critical instability condition for SHPho grooves is reached within this range, while that for HS-grooves is shifted to higher W^+, reflecting enhanced stability induced by wettability heterogeneity.

By introducing the Weber-number-based dimensionless width, the critical condition can be expressed as a critical Weber number W_c^+, which characterizes the transition from quasi-steady to unstable plastron states. Physically, as W^+ approaches W_c^+, the balance between capillary confinement and external hydrodynamic forcing becomes increasingly fragile, leading to a rapid reduction in plastron lifetime. The observed decay trend indicates that the steady-state duration T may scale with the distance between the dimensionless groove width W^+ and the critical instability width W_c^+. The control parameter gap $(W_c^+ - W^+)$ is consistent with a transition governed by the competition between capillary pinning and flow-induced destabilization. Although a quantitative relationship is not established here, the observed trend suggests a possible exponential dependence of the steady-state plastron duration on the distance to the critical condition, which warrants further investigation.

Overall, these results clearly demonstrate that HS-grooves significantly enhance the stability of the plastron, effectively delaying the onset of instability under increasing hydrodynamic forcing.

3.3 Groove Size and Drag Reduction

The underwater frictional drag of HS-grooves with varying geometries was measured using a circulating pipeline system (Fig. 2b). The flow velocity in the test section was maintained at 1.0 m/s, corresponding to a global Reynolds number of $Re = 1.3 \times 10^4$, with the test surface located within a turbulent boundary layer (TBL). The pressure drop between the inlet and outlet of the pipe was used to quantify the frictional drag and associated energy dissipation of the fluid over the

test surface. The drag reduction performance of each sample was evaluated by comparison with a reference surface. The drag reduction ratio (DR) is defined as:

$$DR = \frac{\tau_{\mathrm{C}} - \tau_{\mathrm{E}}}{\tau_{\mathrm{C}}} \times 100\% \tag{4}$$

Where τ_{C} and τ_{E} denote the frictional drag of the control and experimental group, respectively. Let S and S' represent the total inner surface area of the test section and the area of sample, respectively. According to the Fanning equation [33,34], the frictional drag τ_0 along the smooth test section without samples can be expressed in terms of the pressure drop ΔP_0 as:

$$\tau_0 = \frac{1}{2}\rho u^2 f_0 = \frac{\Delta P_0 A}{S} \tag{5}$$

Where f_0 denotes the friction coefficient of the smooth test section. Following the same formulation, the frictional drag for the control and experimental groups can be expressed as:

$$\tau = \frac{\Delta P A - \tau_0 (S - S')}{S'} \tag{6}$$

Where ΔPcorresponds to $\Delta P_C$and ΔP_E for the control and experimental groups, respectively. Based on the pipe configuration and cross-sectional geometry described in Section 2.4, it follows that:

$$S' \approx \frac{1}{3} S \tag{7}$$

Therefore, the drag reduction ratio can be expressed as:

$$DR = \frac{3(\Delta P_C - \Delta P_E)}{3\Delta P_C - 2\Delta P_0} \times 100\% \tag{8}$$

Where ΔP_0 and ΔP_C are constants obtained from repeated measurements and averaging. The measured pressure drop in each experimental run directly enables calculation of the drag reduction performance of the corresponding sample surface. Fig. 4d-f present the drag reduction results of HS-grooves with W^+ values of 6.9, 11.0, 13.7, 16.5, and 20.6 in the pipeline system. The results show that, with other parameters held constant, the drag reduction rate first increases and then

decreases with increasing W^+, with the highest value observed around $W^+ = 13.7$ under the present experimental conditions. In contrast, the drag reduction rate increases monotonically with increasing H/W, reaching its maximum at $H/W = 5$. These trends are consistently observed across all tested S/W conditions. A negative correlation between drag reduction and S/W is also observed, with higher performance achieved at smaller S/W. The maximum drag reduction is achieved at $W^+ = 13.7$, $H/W = 5$, and $S/W = 0.2$, corresponding to a drag reduction rate of 46.4%. The red cylinder in Fig. S7b illustrates the drag reduction performance of partial SHPho grooves. The results demonstrate that HS-grooves provide higher overall drag reduction than SHPho grooves underwater. This enhancement is attributed to the more regular and stable distributed plastron along the HS-grooves, which maintains an effective AWI throughout the experiment. In contrast, gas in SHPho grooves tends to escape more readily to the ridge regions (Fig. S9b-c), causing transient drag fluctuations on the test surface. Therefore, although the overall plastron in SHPho grooves still offers drag reduction, its efficiency is lower than that of HS-grooves, where the gas is regularly confined within the grooves (see Fig. 2d).

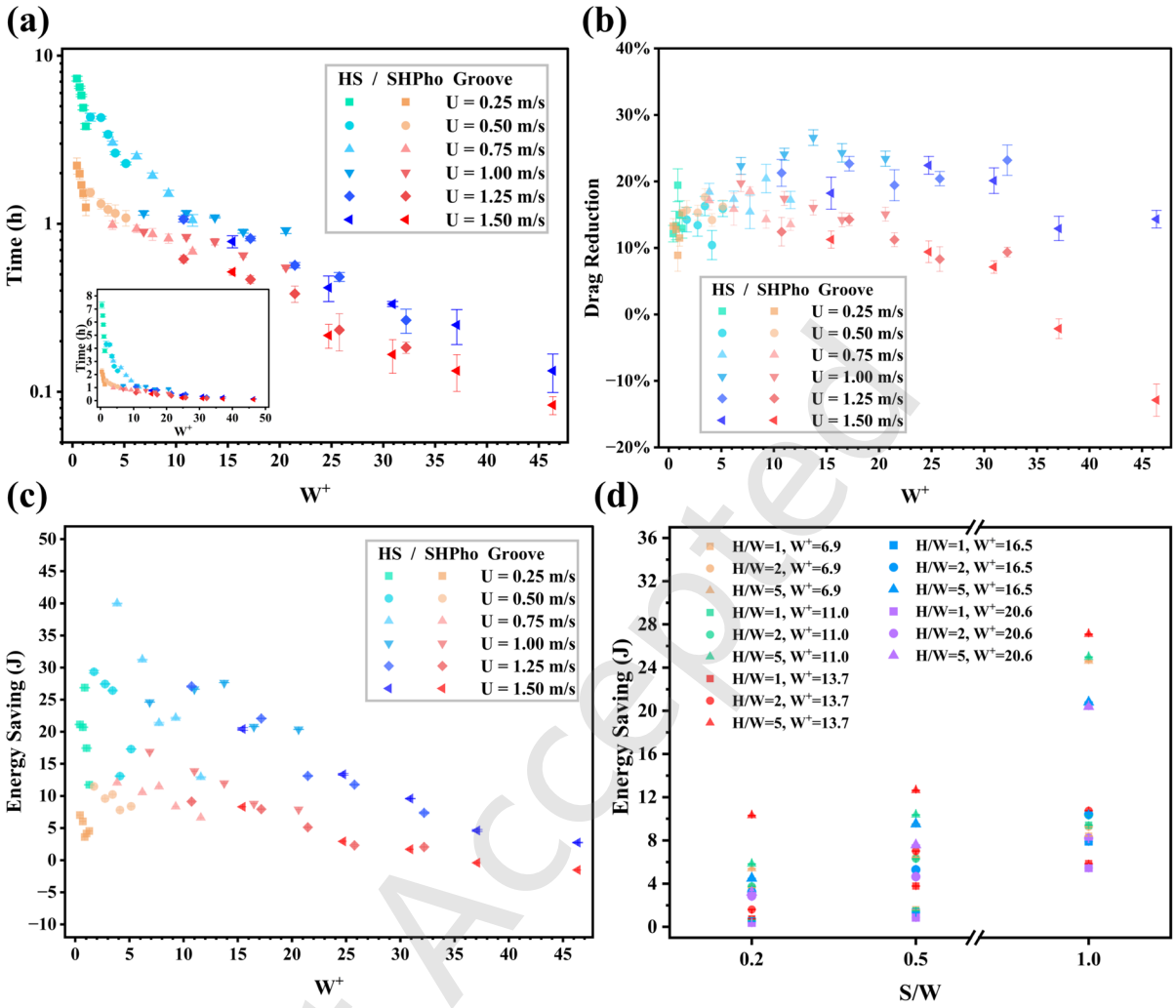

Fig. 5. Variation of (a) plastron steady-state duration, (b) drag reduction rate, and (c) energy saving of grooves with W^+ under the condition of S/W = 1.0 and H/W = 5.0. (d) Variation of energy saving with S/W for all tested HS-grooves with different geometry parameters (specified in the legend).

Fig. S8d-f shows 2D plots of the experimental results. Based on the above analysis, a higher H/W indicates a deeper plastron within the groove, providing sufficient gas volume, mitigating gas loss, and maintaining a stable AWI under flow. This not only prolongs gas retention, as observed in Section 3.2, but also reduces transient frictional fluctuations caused by AWI disturbances. HS-grooves with smaller S/W demonstrate superior drag reduction performance.

This is because a smaller S/W corresponds to a narrower superhydrophilic interval width (S) and a wider superhydrophobic groove width (W) within the same surface area, resulting in a higher proportion of AWI. At the same W^+, a smaller S/W thus increases the AWI area fraction, which enhances the slip effect and positively contributes to drag reduction.

Under identical S/W and H/W, the drag reduction rate first increases and then decreases with increasing W^+, consistent with conventional superhydrophobic behavior [35–37]. Notably, as shown in Fig. 5b, the peak shifts toward a larger W^+ in the presence of heterogeneous wettability, highlighting its stabilizing effect. Increasing W^+ enlarges the AWI area under water, thereby enhancing effective slip and reducing viscous friction compared to solid-liquid interfaces. However, excessively large W^+ promotes plastron destabilization under turbulent flow, ultimately limiting drag reduction performance. When S/W = 1.0, H/W = 5, the SHPho grooves exhibit optimal drag reduction within W^+ = 5 ~ 10, with a maximum drag reduction rate below 20%. In contrast, the HS-grooves shift the optimal performance at a higher W^+ of 10 ~ 15, achieving a significantly enhanced maximum drag reduction exceeding 25%. This shift toward larger characteristic dimensions, coupled with improved peak performance, demonstrates the superior ability of HS-grooves to stabilize the plastron and sustain effective slip under flow conditions. Overall, under otherwise identical conditions, the group of HS-grooves with W^+ = 13.7 achieves the highest drag reduction (26.6%), consistent with the enhanced AWI fraction and plastron stability that promote sustained slip and reduced friction.

As shown in Fig. 4 and Fig. S8, the variation in gas durability with HS-groove geometric parameters does not fully correspond to the trends observed in drag reduction. In particular, the effects of S/W on these two properties exhibits opposite tendencies. To comprehensively assess HS-groove geometries that provide both robust gas durability and effective underwater drag reduction, it is necessary to standardize and unify the relevant physical quantities. Surface

frictional resistance serves as the primary metric for drag reduction, while the practical significance of drag-reducing surfaces ultimately lies in achieving energy savings during actual voyages. Accordingly, for quantitative comparison, the energy savings (E_S) in this study are defined as follows:

$$E_S = M\left(h_{f_C} - h_{f_E}\right) \tag{9}$$

Where M represents the mass of fluid passing through the test surface within a certain period of time, h_{f_C} and h_{f_E} denote the straight-pipe resistance per unit mass of fluid in the control and experimental groups, respectively, with units of J/kg [33,34]. The cross-section area and flow velocity in the two test setups shown in Fig. 2a-b are identical, thus:

$$M = \rho AuT \tag{10}$$

Here, T denotes the experimentally measured steady-state duration of plastron within the groove, as determined according to the Fanning formula:

$$h_f = \lambda\frac{u^2 l}{2d} = \frac{\Delta P}{\rho} \tag{11}$$

Accordingly, we obtain:

$$E_S = \rho AuT\left(\frac{\Delta P_{\mathrm{C}} - \Delta P_{\mathrm{E}}}{\rho}\right) = AuT \cdot DR(3\Delta P_C - \frac{2}{3}\Delta P_0) \tag{12}$$

In summary, the steady-state duration (T) of plastron within the HS-groove and its pipeline drag reduction ratio (DR) are integrated into the definition of the energy-saving index (E_S, unit: J). Although not strictly a quantitative thermodynamic measure, E_S represents a time-weighted, qualitative estimate of frictional energy dissipation reduction, by combining the averaged drag reduction over a representative steady measurement window (~30 s) with the plastron steady-state duration. It therefore characterizes the effective energy-saving capability during sustained gas retention within the HS-grooves, and is primarily suitable for relative comparison under identical experimental conditions. As shown in Fig. 5c, consistent with the observed drag reduction trends,

HS-grooves enable stable gas retention over extended periods at larger W^+, thereby maintaining effective drag reduction and improving energy efficiency. In comparison, the energy saving achieved by HS-grooves is significantly higher than that of conventional SHPho grooves. Furthermore, it renders the evaluation of the optimal HS-groove size more intuitive and straightforward. As shown in Fig. 4g-i and Fig. 5d, for HS-grooves with various W^+, larger S/W and H/W both enhance energy savings, thereby providing guidance for selecting the optimal groove dimension. Under relatively high flow velocity conditions (u = 1.0 m/s) in Fig. 4g-i, the optimal energy-saving index is achieved at W^+ = 13.7, S/W = 1.0, and H/W = 5, corresponding to an E_S of 27.1 J. Although higher E_S values may be obtained at lower flow velocities, such conditions are less relevant to realistic operating scenarios.

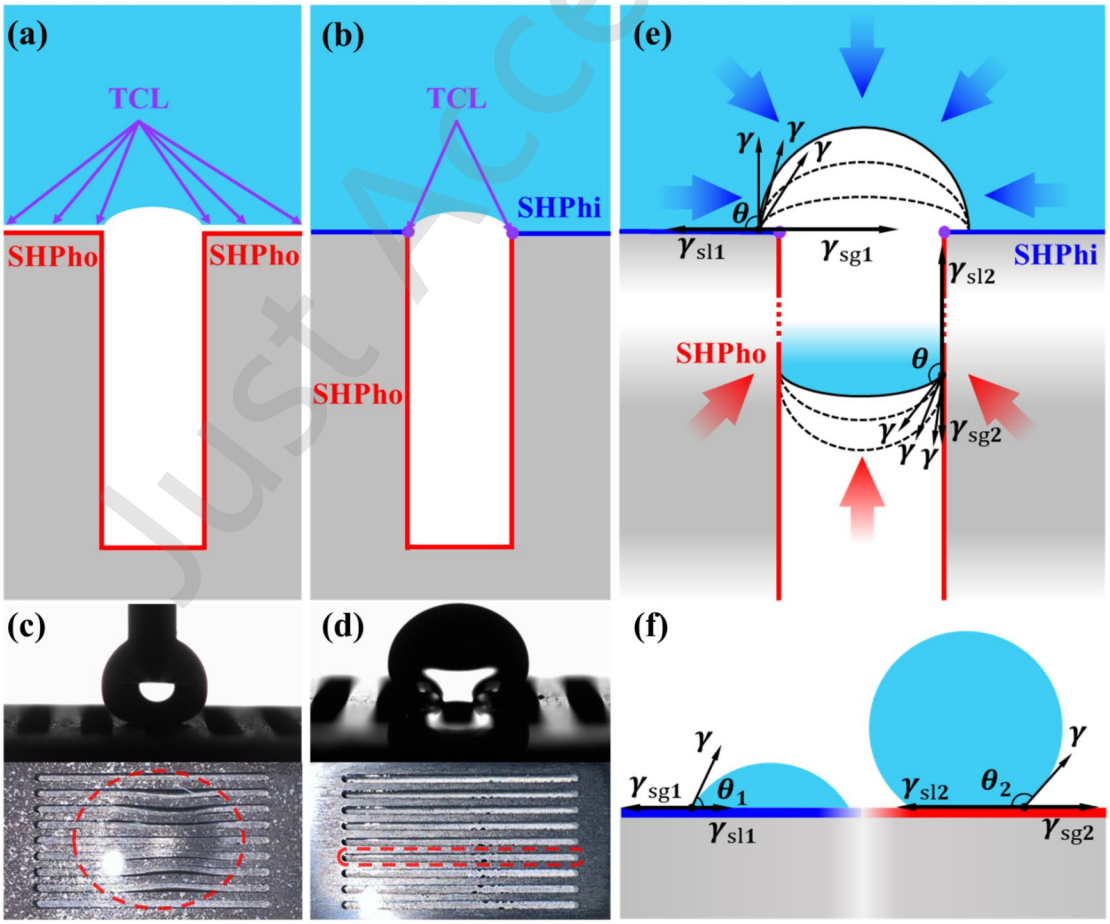

Fig. 6. AWI states on surfaces with heterogeneous superwettability. TCL on (a) a SHPho groove and (b) an HS-groove. Wetting states of droplets in air and bubbles in water on (c) SHPho grooves and (d) HS-groove. Surface tension of the TCL on (e) HS-groove underwater and (f) superhydrophilic/superhydrophobic surfaces in the air.

3.4 Anchoring Effect and Drag Reduction

The primary causes of underwater plastron dissipation on superhydrophobic surfaces include flow shear [38], pressure pulsation [39], gas dissolution [40], and the degradation of superhydrophobic surfaces [13]. These factors typically do not occur independently but rather act in a coupled manner. SHPho grooves can preserve and retain the internal gas through their geometric structure, thereby mitigating the influence of these factors [41]. However, under prolonged turbulent flow conditions, it is challenging for fully SHPho grooves to maintain a stable AWI within the grooves [36]. As shown in Fig. 6a and 6c, the solid-liquid-gas TCL slides along the superhydrophobic surface, causing the plastron to extend beyond the groove interior and spread over the upper surface between the grooves until forming a continuous gas layer (red dashed line in Fig. 6c). In fact, while this configuration may be advantageous for drag reduction under ideal laminar flow, the irregular plastron can generate additional form drag in turbulent flow, as shown in Fig. S9b-c. More critically, the unrestricted movement and exposure of the TCL increase its susceptibility to gas dissipation under complex pressure and shear forces, while the fragile plastron simultaneously accelerates gas dissolution and the transition of the plastron to an unsteady state. HS-grooves can significantly mitigate the adverse effects of TCL slip. As schematically illustrated in Fig. 6a-b and 6e, the wettability transition between the superhydrophobic groove interior and the superhydrophilic top surface introduces a distinct surface energy barrier at the groove edge, which anchors the TCL. This anchoring effect can be interpreted as a restoring force arising from the imbalance of surface tension components along the contact line, quantitatively scaling with

$\sigma(cos\theta_{SHPhi} - cos\theta_{SHPho})$. Owing to the strong surface energy barrier induced by the wettability transition, the TCL of HS-grooves is anchored at the groove top. As shown in Fig. 6b, 6d, and 6e, when the curved AWI tends to move downward due to pressure and gas dissolution, the superhydrophobic inner wall of the groove exerts an upward force at the contact line (red arrow), which, together with the pressure of compressed gas, drives the AWI upward. If the AWI encounters local low pressure or other factors leading to air escape or precipitation, the superhydrophilic surface between grooves exerts surface forces toward the groove (blue arrow), thereby confining the AWI to the groove region. Consequently, the AWI is anchored at the transition boundary between the superhydrophilic and superhydrophobic regions at the groove edge (purple point in the cross-section of Fig. 6b and 6e). The enhanced stability induced by heterogeneous superwettability can be quantitatively analyzed through surface tension-based pinning forces. For superhydrophobic surfaces, the pinning force per unit length is expressed as [42,43]:

$$F_{pin,SHPho} = \sigma \Delta cos\theta_{SHPho} \tag{13}$$

Where $\Delta cos\theta_{SHPho}$ denotes the contact angle hysteresis of the superhydrophobic surface. The relationship between the hysteresis and the roll-off angle α is given by:

$$mgsin\alpha = k\sigma w \Delta cos\theta_{SHPho} \tag{14}$$

Here, m is the droplet mass, g is the gravitational acceleration, k is a geometric coefficient (commonly taken as 1), and w denotes the droplet contact diameter, which can be calculated from the droplet volume V as [44]:

$$V = \frac{\pi w^3}{6} \frac{(1 - cos\theta_{SHPho})^2 (2 + cos\theta_{SHPho})}{sin^3 \theta_{SHPho}} \tag{15}$$

For a droplet with V = 5 uL on a superhydrophobic surface (θ_{SHPho} = 160.6°, α = 2.0°), the pinning force is calculated as:

$$F_{pin,SHPho} = 3.85 \times 10^{-3} \text{ N/m} \tag{16}$$

For surfaces with heterogeneous superwettability, the pinning force per unit length becomes [45,46]:

$$F_{pin,HS} = \sigma(cos\theta_{SHPhi} - cos\theta_{SHPho}) \quad (17)$$

Where θ_{SHPhi} represents the superhydrophilic contact angle, approximated as 0° ($cos\theta_{SHPhi} \approx 1$). Substituting the relevant values yields:

$$F_{pin,SHPho} = 1.41 \times 10^{-1}\ \text{N/m} \quad (18)$$

This corresponds to an enhancement of nearly 40-fold relative to the superhydrophobic surface, which directly reflects the much stronger surface energy barrier at the wettability transition boundary, thereby effectively anchoring the TCL and suppressing its lateral displacement under flow-induced shear and pressure fluctuations, explaining the superior gas retention stability of HS-grooves under water.

The macroscopic behavior of water droplets on the grooves indirectly illustrates the distinct properties of the two groove types. As shown in Fig. 6c, due to the superhydrophobicity of the upper surfaces between the SHPho grooves, water droplets cannot easily wet or anchor on the groove top. Consequently, the grooves also struggle to retain gas underwater. In contrast, for HS-grooves, only the groove interiors are superhydrophobic, whereas the upper surfaces between the grooves are superhydrophilic. As shown in Fig. 6d, water droplets are adsorbed above the groove like a lid without penetrating into it, thereby trapping air inside the grooves.

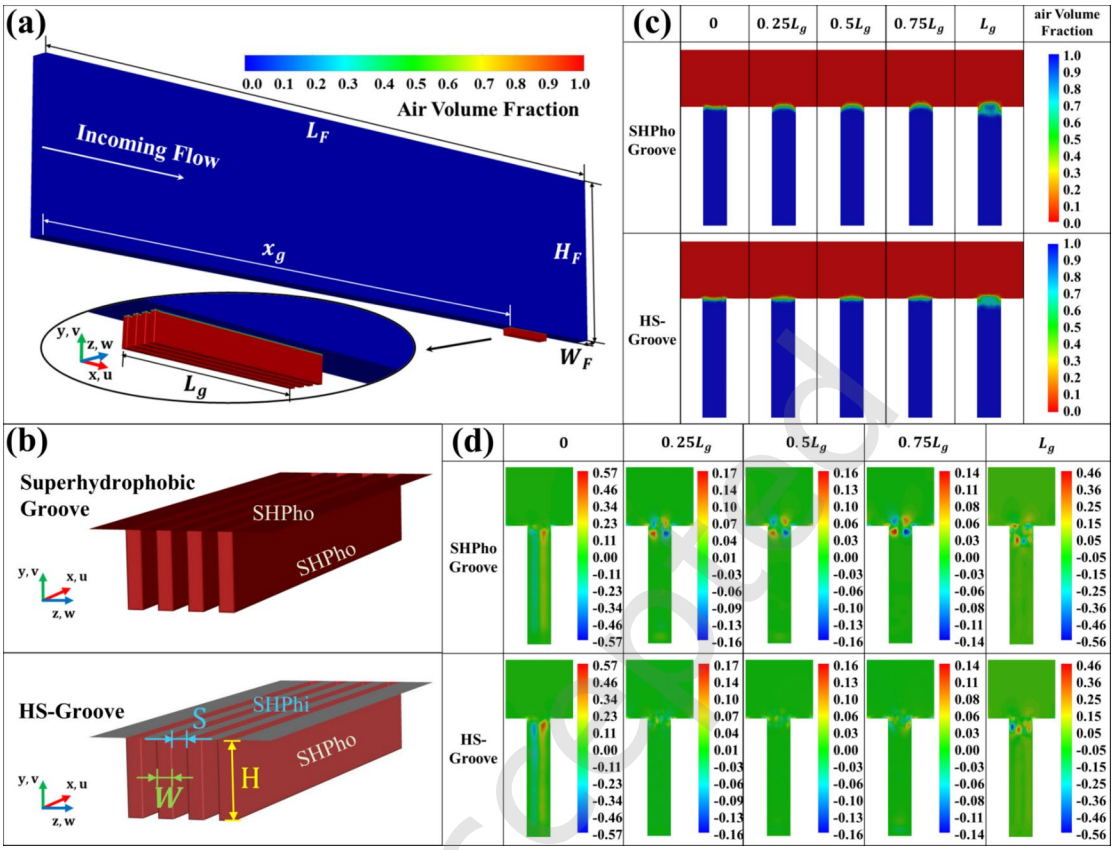

Fig. 7. CFD simulations of grooves. (a) Computational domain and (b) groove region in the simulation. Distributions of (c) air volume fraction and (d) velocity component w in the cross-section of the groove region.

Superhydrophobic grooves are known to exhibit underwater drag reduction performance [15]. This occurs because the plastron on the superhydrophobic surface facilitates streamwise slip, thereby reducing velocity gradients and suppressing turbulence. As shown in Fig. 4, certain HS-grooves exhibited superior drag reduction performance in the pipeline tests. This improvement is partly attributed to the more stable air layer in the HS-groove, which ensures more effective slip at the AWI. Furthermore, the spatial arrangement of the superhydrophilic and superhydrophobic phases suppresses spanwise flow and secondary vortex formation.

Based on the groove of $H/W = 5$, $S/W = 0.2$, and $W^+ = 13.7$, the above findings were further verified using computational fluid dynamics simulation. As shown in Fig. 7a-b, computational

domains were established for both the HS-groove and the SHPho groove. The total frictional resistance of the bottom surface for the two groove types, along with a control group (a smooth bottom wall without grooves under the same flow field), was calculated using Equation (3) to determine the drag reduction rate. The drag reduction rate of the HS-groove was 30.3% (compared to 26.6% in the experiment), whereas that of the SHPho groove was 18.6% (16.1% experimentally). The simulations indicate that at an incoming flow velocity of U = 1.0 m/s, both grooves reduce resistance, with the HS-groove exhibiting superior drag reduction compared to the SHPho groove. Fig. 8 shows the distribution of the normalized flow velocity profile ($u' = u/U$) along the flow domain. The vertical coordinate of the velocity profile is y' ($= y/H_f$). This figure reflects the relationship between flow velocity and height at different streamwise (x direction) positions in the flow field. The blue region in Fig. 8a-b represents the flow development stage from the inlet to the front edge of the groove, where a gradual increase in boundary layer thickness ($\delta = y_{0.99U}$) can be observed. As the flow passes through the green region where the groove is located, the velocity gradient decreases significantly, streamwise slip appears, and this slip intensifies downstream. Upon reaching the end of the groove region, the velocity gradient suddenly increases, the slip diminishes, and the original velocity gradient is restored in the downstream section (red region). This explains the flow-field mechanism underlying drag reduction in SHPho grooves. The AWI within the groove provides effective streamwise slip, thereby reducing shear stress associated with the velocity gradient and consequently lowering drag [47]. The HS-groove generates more pronounced streamwise slip than the SHPho groove, as clearly illustrated in Fig. 8c. This figure presents the magnified view of the groove and uses the velocity profile at the flow-development section (x = 300 mm) as a reference. The reference velocity profile exhibits no apparent streamwise slip, whereas slip occurs in both the SHPho groove and the HS-groove and gradually intensifies along the streamwise direction. The HS-groove provides more substantial streamwise

slip, explaining why its drag reduction rate is higher than that of the SHPho groove.

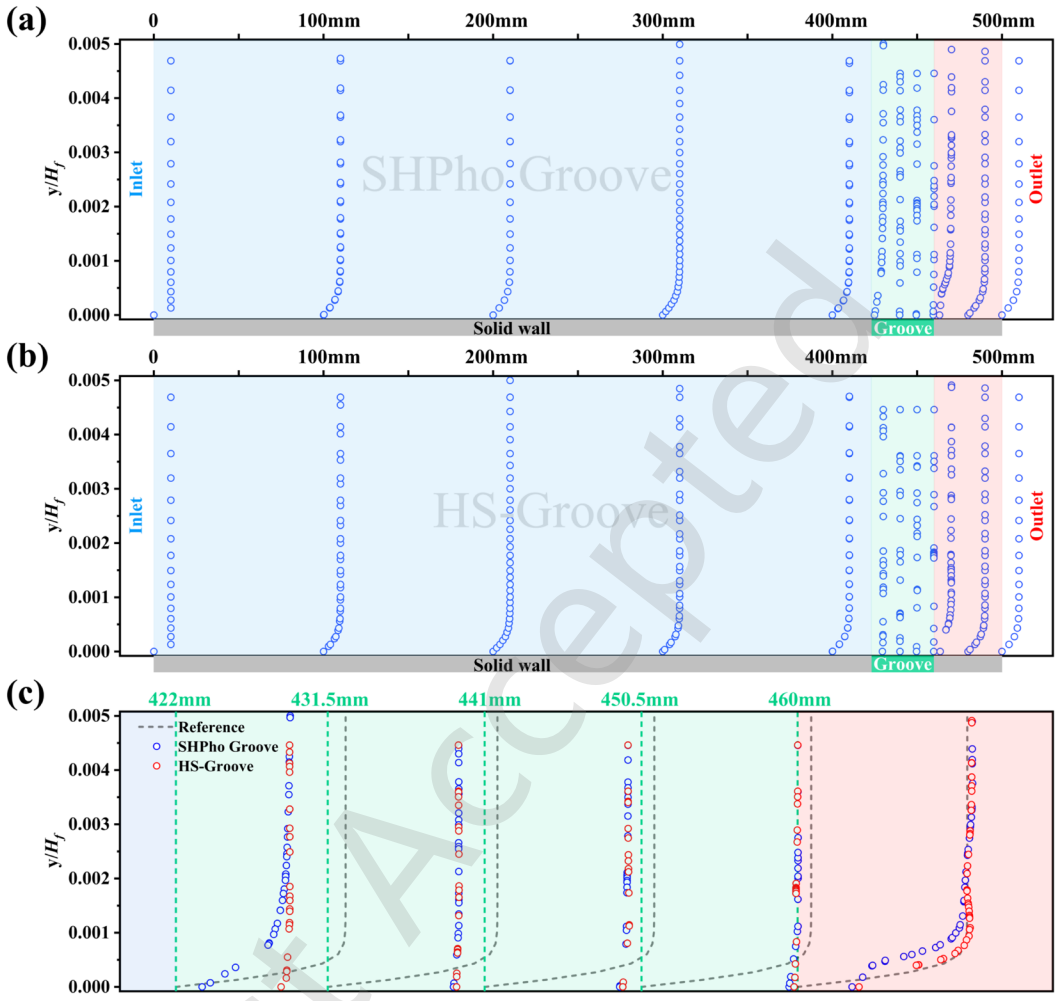

Fig. 8. Streamwise velocity profiles (y'-u') along the flow direction. y'-u' at various x-positions in the entire flow domain for (a) the SHPho groove and (b) the HS-groove. (c) y'-u' at various x-positions within the groove region.

Furthermore, under the influence of the flow field, the HS-groove more effectively preserves both the relative position and the morphology of the AWI. Fig. 7c presents the distribution of the air volume fraction in the cross-section (YZ plane) of the groove region. The air volume fraction contours, from the upstream start ($x = x_g$) to the downstream end ($x = x_g + L_g$), reveal that in the SHPho groove, the AWI is upwardly curved, with the TCL lying below the groove edge and

gradually decreasing along the flow direction. This partial exposure of the groove to the flow field is unfavorable for drag reduction. In contrast, the AWI of the HS-groove remains anchored at the groove top, forming a nearly planar interface that aligns with the bottom of the flow field. This suggests that the superwettability transition stabilizes both the position and morphology of the AWI under flow condition. Furthermore, the cross-sectional (YZ plane) distribution of the spanwise velocity (w, in the z-direction) within the groove region is analyzed. As shown in Fig. 7d, a pronounced spanwise velocity distribution is observed around the AWI in the SHPho groove. The symmetry and opposite distribution of w indicates the formation of vortices in this region. This results from secondary vortices induced by the nonuniform distribution of streamwise velocity u along the z-direction, which limits the drag reduction performance of the superhydrophobic surface. In contrast, the HS-groove exhibits minimal spanwise flow, largely confined beneath the AWI (air flow), thereby reducing non-streamwise momentum loss. This behavior arises from the heterogeneous superwettability, where superhydrophilic and superhydrophobic strips aligned with the flow direction confine the flow into discrete channels, effectively suppressing transverse motion and secondary vortex formation. To further quantify this effect, the streamwise (x-direction) vorticity (associated with spanwise vortex structures) distributions at multiple streamwise locations are provided in Fig. S13. The HS-groove exhibits an approximately 50% reduction in peak vorticity compared to the superhydrophobic groove across all examined sections, demonstrating a significant suppression of spanwise vortex structures. This reduced vorticity is consistent with the weakened transverse flow observed in Fig. 7d and indicates diminished transverse momentum transport.

These results elucidate the mechanism underlying the superior drag reduction of the HS-groove. The spatially heterogeneous wettability not only stabilizes the AWI by anchoring the plastron and enhancing streamwise slip, but also suppresses spanwise flow via the surface energy

barrier, thereby reducing vortex-induced energy dissipation.

4 Conclusion

In conclusion, this study successfully fabricated HS-grooves featuring a superhydrophobic interior and a superhydrophilic top surface. Both the superhydrophilic and superhydrophobic surfaces exhibited excellent extreme wettability and durability. The microstructures and physicochemical properties of the two extreme-wettability surfaces were systematically characterized and compared, thereby ensuring the feasibility of achieving superwettability transitions on the same substrate. Experimental results demonstrated that HS-grooves exhibit superior underwater plastron anchoring capability, with a steady-state plastron duration of up to 7.3 h ($W^+ = 0.43$, $S/W = 1.0$, $H/W = 5.0$), which is approximately 5.1 h longer than that of SHPho grooves under identical conditions. Owing to their excellent plastron stability and durable AWI, HS-grooves exhibited outstanding drag reduction performance in the pipeline, achieving a maximum drag reduction rate of 46.4%. This performance surpasses that of purely superhydrophobic grooves and is superior to the drag reduction rates reported for most superhydrophobic grooved surfaces in pipe-flow test systems. A comprehensive evaluation of plastron durability and drag reduction performance across HS-grooves of varying geometries was conducted, and the optimal groove dimensions were identified through comparative analysis of total energy savings. The underwater plastron anchoring effect of HS-grooves was analyzed from the perspective of surface energy barriers, and the drag reduction mechanism was further verified through computational fluid dynamics simulations. HS-grooves promote sustained interfacial slip while constraining transverse momentum exchange, thereby reducing vortex-induced dissipation. This work presents a feasible and reliable surface-engineering strategy for maintaining the underwater AWI and reducing frictional drag, offering significant guidance and practical application potential for drag reduction in underwater equipment, while further studies are needed

to assess long-term performance under realistic marine service conditions.

Acknowledgements

None.

Author contribution statement

Zhitao Huang: conceptualization, methodology, validation, formal analysis, investigation, writing – original draft, and visualization. Yiwei Hu: validation, and visualization. Zhaoxi Liang: investigation. Shicai Zhu: methodology and formal analysis. Liran Ma: conceptualization, writing – review & editing, supervision, project administration, and funding acquisition. Jianbin Luo: writing – review & editing, supervision. All the authors have approved the final manuscript.

Data availability

The data that support the findings of this study is available from the corresponding author upon reasonable request.

Declaration of competing interest

All the contributing authors report no conflicts of interest in this work.

Funding

This work was supported by the National Natural Science Foundation of China (No.52488101), and the Fundamental and Interdisciplinary Disciplines Breakthrough Plan of the Ministry of Education of China (No. JYB2025XDXM209).

Use of AI statement

None.

Supplementary materials: Supplementary material (further details of substrate fabrication and chemical modification (oxidation, silane treatment), surface characterization (XPS, SEM, EDS, optical microscopy, white-light interferometry), wettability measurements (contact angle, rolling angle); durability evaluation (flow scouring, abrasion tests), drag reduction experiments and numerical simulation (ANSYS Fluent)) is available in the online version of this article at https://doi.org/10.26599/OCEAN.2026.9470024

References

[1] M. Zaman Khan, J. Militky, M. Petru, B. Tomková, A. Ali, E. Tören, S. Perveen, Recent advances in superhydrophobic surfaces for practical applications: a review, Eur. Polym. J. 178 (2022) 111481. https://doi.org/10.1016/j.eurpolymj.2022.111481.

[2] M. Beitollahpoor, M. Farzam, N.S. Pesika, Friction force-based measurements for simultaneous determination of the wetting properties and stability of superhydrophobic surfaces, J. Colloid Interface Sci. 648 (2023) 161–168. https://doi.org/10.1016/j.jcis.2023.05.161.

[3] H. Xie, J. Wei, S. Duan, Q. Zhu, Y. Yang, K. Chen, J. Zhang, L. Li, J. Zhang, Non-fluorinated and durable photothermal superhydrophobic coatings based on attapulgite nanorods for efficient anti-icing and deicing, Chem. Eng. J. 428 (2022) 132585. https://doi.org/10.1016/j.cej.2021.132585.

[4] Z. Huang, S. Zhu, M. Zhu, Y. Tian, L. Ma, A durable superhydrophobic surface with bud-particle structure prepared by one-step spray method, Appl. Surf. Sci. 679 (2025) 161255. https://doi.org/10.1016/j.apsusc.2024.161255.

[5] L. Xin, H. Li, J. Gao, Z. Wang, K. Zhou, S. Yu, Large-scale fabrication of decoupling coatings with promising robustness and superhydrophobicity for antifouling, drag reduction, and organic photodegradation, Friction 11 (2023) 716–736. https://doi.org/10.1007/s40544-022-0652-3.

[6] C. Lee, C.-H. Choi, C.-J. Kim, Superhydrophobic drag reduction in laminar flows: a critical review, Exp. Fluids 57 (2016) 176. https://doi.org/10.1007/s00348-016-2264-z.

[7] Z.Q. Tang, T. Tian, P.J. Molino, A. Skvortsov, D. Ruan, J. Ding, Y. Li, Recent advances in superhydrophobic materials development for maritime applications, Adv. Sci. 11 (2024) 2308152. https://doi.org/10.1002/advs.202308152.

[8] L. Zhang, W. Zhou, C.R. Crick, H.C.-H. Ng, R.J. Poole, Slip length and drag reduction of superhydrophobic surfaces in shear-thinning fluid flows, J. Colloid Interface Sci. 685 (2025) 468–475. https://doi.org/10.1016/j.jcis.2025.01.152.

[9] Z. Wang, X. Liu, J. Ji, T. Tao, T. Zhang, J. Xu, Y. Jiao, K. Liu, Underwater drag reduction and buoyancy enhancement on biomimetic antiabrasive superhydrophobic coatings, ACS Appl. Mater. Interfaces 13 (2021) 48270–48280. https://doi.org/10.1021/acsami.1c14342.

[10] N.J. Shirtcliffe, G. McHale, M.I. Newton, C.C. Perry, F.B. Pyatt, Plastron properties of a superhydrophobic surface, Appl. Phys. Lett. 89 (2006) 104106. https://doi.org/10.1063/1.2347266.

[11] G. McHale, M.R. Flynn, M.I. Newton, Plastron induced drag reduction and increased slip on a superhydrophobic sphere, Soft Matter 7 (2011) 10100–10107. https://doi.org/10.1039/C1SM06140B.

[12] G. McHale, N.J. Shirtcliffe, C.R. Evans, M.I. Newton, Terminal velocity and drag reduction measurements on superhydrophobic spheres, Appl. Phys. Lett. 94 (2009) 64104. https://doi.org/10.1063/1.3081420.

[13] D. Wang, Q. Sun, M.J. Hokkanen, C. Zhang, F.-Y. Lin, Q. Liu, S.-P. Zhu, T. Zhou, Q. Chang, B. He, Q. Zhou, L. Chen, Z. Wang, R.H.A. Ras, X. Deng, Design of robust superhydrophobic surfaces, Nature 582 (2020) 55–59. https://doi.org/10.1038/s41586-020-2331-8.

[14] Q. Dai, L. Chen, J. Pan, L. Shi, D. Liu, W. Huang, X. Wang, Rapid surface texturing to achieve robust superhydrophobicity, controllable droplet impact, and anti-frosting performances, Friction 12 (2024) 291–304. https://doi.org/10.1007/s40544-023-0757-3.

[15] Y. Nie, Y. Zhang, D. Weng, J. Wang, Drag reduction and air restoration of streamwise hydrophobic microtrenches, Phys. Fluids 37 (2025) 75130. https://doi.org/10.1063/5.0275156.

[16] A.A. Hemeda, H. Vahedi Tafreshi, Instantaneous slip length in superhydrophobic microchannels having grooves with curved or dissimilar walls, Phys. Fluids 27 (2015) 102101. https://doi.org/10.1063/1.4931588.

[17] L. Speichermann-Jägel, S. Dullenkopf-Beck, R. Droll, D. Gandyra, M. Barczewski, S. Walheim, T. Schimmel, Stable air retention under water on artificial salvinia surfaces enabled by the air spring effect: the importance of geometrical and surface-energy barriers, and of the air spring height, Adv. Mater. Interfaces 11 (2024) 2400400. https://doi.org/10.1002/admi.202400400.

[18] H. Hu, J. Wen, L. Bao, L. Jia, D. Song, B. Song, G. Pan, M. Scaraggi, D. Dini, Q. Xue, F. Zhou, Significant and stable drag reduction with air rings confined by alternated superhydrophobic and hydrophilic strips, Sci. Adv. 3 (2017) e1603288. https://doi.org/10.1126/sciadv.1603288.

[19] B. Wang, Y. Zhang, L. Shi, J. Li, Z. Guo, Advances in the theory of superhydrophobic surfaces, J. Mater. Chem. 22 (2012) 20112. https://doi.org/10.1039/c2jm32780e.

[20] H.-J. Butt, J. Liu, K. Koynov, B. Straub, C. Hinduja, I. Roismann, R. Berger, X. Li, D. Vollmer, W. Steffen, M. Kappl, Contact angle hysteresis, Curr. Opin. Colloid Interface Sci. 59 (2022) 101574. https://doi.org/10.1016/j.cocis.2022.101574.

[21] M. Li, A. Mao, Q. Guan, E. Saiz, Nature-inspired adhesive systems, Chem. Soc. Rev. 53 (2024) 8240–8305. https://doi.org/10.1039/D3CS00764B.

[22] L. Li, J. Zhu, Z. Zeng, E. Liu, Q. Xue, Effect of surface roughness on the angular acceleration for a droplet on a super-hydrophobic surface, Friction 9 (2021) 1012–1024. https://doi.org/10.1007/s40544-020-0392-1.

[23] L. Zhu, Y. Guan, Y. Wang, Z. Xie, J. Lin, J. Zhai, Influence of process parameters of ultrasonic shot peening on surface roughness and hydrophilicity of pure titanium, Surf. Coat. Technol. 317 (2017) 38–53. https://doi.org/10.1016/j.surfcoat.2017.03.044.

[24] Y.-H. Chang, Y.-T. Huang, M.K. Lo, C.-F. Lin, C.-M. Chen, S.-P. Feng, Electrochemical fabrication of transparent nickel hydroxide nanostructures with tunable superhydrophobicity/superhydrophilicity for 2D microchannels application, J. Mater, Chem, A 2 (2014) 1985–1990. https://doi.org/10.1039/C3TA13882H.

[25] A. Skarmoutsou, C.A. Charitidis, A.K. Gnanappa, A. Tserepi, E. Gogolides, Nanomechanical and nanotribological properties of plasma nanotextured superhydrophilic and superhydrophobic polymeric surfaces, Nanotechnology 23 (2012) 505711. https://doi.org/10.1088/0957-4484/23/50/505711.

[26] S. Keshavarzi, G. Momen, P. Eberle, A. Azimi Yancheshme, N.J. Alvarez, R. Jafari, Exploiting intermediate wetting on superhydrophobic surfaces for efficient icing prevention, J. Colloid Interface Sci. 670 (2024) 550–562. https://doi.org/10.1016/j.jcis.2024.05.068.

[27] Z. Su, C. Ye, Y. Xu, B. Wu, D.-H. Kuo, X. Wu, B. Yang, P. Zhang, L. Chen, D. Lu, J. Lin, Z. Yuan, X. Chen, Synergistic vacancy defects and the surface hydrophobic-to-superhydrophilic wetting engineering in W/S co-doped BiOI for enhanced photocatalytic hydrogen evolution, Chem. Eng. J. 496 (2024) 154282. https://doi.org/10.1016/j.cej.2024.154282.

[28] C. Yao, J. Zhang, Z. Xue, K. Yu, X. Yu, X. Yang, Q. Qu, W. Gan, J. Wang, L. Jiang, Bioinspired cavity regulation on superhydrophobic spheres for drag reduction in an aqueous medium, ACS Appl. Mater. Interfaces 13 (2021) 4796–4803. https://doi.org/10.1021/acsami.0c20073.

[29] Y.N. Teja, M. Sakar, K. Vinothkumar, R.G. Balakrishna, Large scale synthesis of silane functionalized near-superhydrophobic aluminium hydroxide particles via facile surface grafting technique, Mater. Today Commun. 26 (2021) 101744. https://doi.org/10.1016/j.mtcomm.2020.101744.

[30] S. Tugulu, K. Löwe, D. Scharnweber, F. Schlottig, Preparation of superhydrophilic microrough titanium implant surfaces by alkali treatment, J. Mater. Sci.: Mater. Med. 21 (2010) 2751–2763. https://doi.org/10.1007/s10856-010-4138-x.

[31] J. Xu, I.-Y. Jeon, H.-J. Choi, S.-J. Kim, S.-H. Shin, N. Park, L. Dai, J.-B. Baek, Metalated graphene nanoplatelets and their uses as anode materials for lithium-ion batteries, 2D Mater. 4 (2016) 14002. https://doi.org/10.1088/2053-1583/4/1/014002.

[32] M. Thiagarajan, K. Iyakutti, E. Palaniyandi, M. Mahendran, Electronic structure of al, P, S, and cl impurities in silicon, Int. J. Quantum Chem. 58 (1998) 383–388. https://doi.org/10.1002/(SICI)1097-461X(1996)58:4%253C383::AID-QUA7%253E3.0.CO;2-U.

[33] I.T. Dosunmu, S.N. Shah, Turbulent flow behavior of surfactant solutions in straight pipes, J. Pet. Sci. Eng. 124 (2014) 323–330. https://doi.org/10.1016/j.petrol.2014.09.025.

[34] Y. Yuan, R. Yin, J. Jing, S. Du, J. Pan, Establishment of a reynolds average simulation method and study of a drag reduction mechanism for viscoelastic fluid turbulence, Phys. Fluids 35 (2023) 15146. https://doi.org/10.1063/5.0138491.

[35] M. Xu, N. Yu, J. Kim, C.-J. "Cj" Kim, Superhydrophobic drag reduction in high-speed towing tank, J. Fluid Mech. 908 (2021) A6. https://doi.org/10.1017/jfm.2020.872.

[36] H. Park, C.-H. Choi, C.-J. Kim, Superhydrophobic drag reduction in turbulent flows: a critical review, Exp. Fluids 62 (2021) 229. https://doi.org/10.1007/s00348-021-03322-4.

[37] W. Abu Rowin, J. Hou, S. Ghaemi, Turbulent channel flow over riblets with superhydrophobic coating, Exp. Therm Fluid Sci. 94 (2018) 192–204. https://doi.org/10.1016/j.expthermflusci.2018.02.001.

[38] H.J. Park, Y. Tasaka, Y. Oishi, Y. Murai, Drag reduction promoted by repetitive bubble injection in turbulent channel flows, Int. J. Multiphase Flow 75 (2015) 12–25. https://doi.org/10.1016/j.ijmultiphaseflow.2015.05.003.

[39] A. Bussonnière, Q.C. Liu, P.A. Tsai, Acoustic responses of underwater superhydrophobic surfaces subjected to an intense pulse, J. Fluid Mech. 956 (2023) A32. https://doi.org/10.1017/jfm.2023.61.

[40] D. Panchanathan, A. Rajappan, K.K. Varanasi, G.H. McKinley, Plastron regeneration on submerged superhydrophobic surfaces using in situ gas generation by chemical reaction, ACS Appl. Mater. Interfaces 10 (2018) 33684–33692. https://doi.org/10.1021/acsami.8b12471.

[41] P. Du, J. Wen, Z. Zhang, D. Song, A. Ouahsine, H. Hu, Maintenance of air layer and drag reduction on superhydrophobic surface, Ocean Eng. 130 (2017) 328–335. https://doi.org/10.1016/j.oceaneng.2016.11.028.

[42] C.G.L. Furmidge, Studies at phase interfaces. I. The sliding of liquid drops on solid surfaces and a theory for spray retention, J. Colloid Sci. 17 (1962) 309–324. https://doi.org/10.1016/0095-8522(62)90011-9.

[43] H. Chen, T. Tang, H. Zhao, K.-Y. Law, A. Amirfazli, How pinning and contact angle hysteresis govern quasi-static liquid drop transfer, Soft Matter 12 (2016) 1998–2008. https://doi.org/10.1039/C5SM02451J.

[44] W.T. Leung, A study of the detachment of droplets from a clean surface, Ph.D., The Hong Kong University of Science and Technology, 2016. https://doi.org/10.14711/thesis-b1750037.

[45] H. Kusudo, T. Omori, Y. Yamaguchi, Extraction of the equilibrium pinning force on a contact line exerted from a wettability boundary of a solid surface through the connection between mechanical and thermodynamic routes, J. Chem. Phys. 151 (2019) 154501. https://doi.org/10.1063/1.5124014.

[46] H. Barrio-Zhang, É. Ruiz-Gutiérrez, S. Armstrong, G. McHale, G.G. Wells, R. Ledesma-Aguilar, Contact-angle hysteresis and contact-line friction on slippery liquid-like surfaces, Langmuir 36 (2020) 15094–15101. https://doi.org/10.1021/acs.langmuir.0c02668.

[47] A. Kitagawa, Y. Shiomi, Y. Murai, P. Denissenko, Transient velocity profiles and drag reduction due to air-filled superhydrophobic grooves, Exp Fluids 61 (2020) 237. https://doi.org/10.1007/s00348-020-03070-x.